



LUND
UNIVERSITY

DEPARTMENT OF PHYSICS
DIVISION OF NUCLEAR PHYSICS
BACHELOR OF SCIENCE THESIS

**Dead layer determination for the new
implantation detector of the LUNDIUM decay
station**

Author: Eleftheria Kosta

Supervisor:
Luis Sarmiento
Co-supervisor:
Daniel Cox

ACADEMIC TERM: AUTUMN 2021

January 20, 2022

Abstract

The Nuclear Structure Group in Lund, focuses on nuclear spectroscopy of decays of rare isotopes. A new decay station, called LUNDIUM, is currently being built, which will involve silicon and germanium detectors for the study of these nuclei. This thesis focuses on the characterization of one of the new silicon detectors, the implantation one. More specifically, the dead layer is determined over the entire surface of the detector. The silicon detector is ion-implanted and silicon dioxide passivated, forming the dead layer, which is unable to record the energies of the particles passing through. Superheavy elements decay by alpha decay, and the energy registered on the detectors from the alpha particles depends on the amount of material that they have to pass through. By knowing the thickness of the dead layer, the full energy of the particles can be reconstructed. During superheavy experiments, the compound nucleus is implanted in the implantation detector. The dead layer plays a significant role in correcting the energy emission of the particles that escape the implantation detector and are stopped in one of the box detectors. For the dead layer thickness determination, data with two alpha sources ^{148}Gd and ^{244}Cm , as well as an electron source ^{133}Ba were taken and analyzed. The dead layer was found to be in the order of $0.6\text{ }\mu\text{m}$.

Popular Abstract

A part of nuclear physics focuses on superheavy elements at the higher end of periodic table. The creation of superheavy elements is as fascinating as it sounds and it involves a sequence of work in order to be achieved. In Lund, the most up-to-date decay station is currently being built, focusing on decay spectroscopy of these exotic nuclei. These synthetically created superheavy elements, are studied by the detection of their decay products. For their detection, high quality detectors are used. This thesis focuses on the characterization of the implantation detector, which is a silicon detector responsible for detecting charged particles. The thickness of the dead layer over the surface of the detector is determined. This dead layer is a mixture of ion-implanted, aluminium and silicon dioxide and it is unable to record the energies of the particles passing through. By knowing the thickness of it, the true emission energy of the particles can be reconstructed. In our lab, the silicon detector is called DSSSD, which stands for Double-Sided Silicon-Strip Detector and it has 58 horizontal and 58 vertical strips, creating a 2-Dimensional surface with a total of 3364 pixels. In order to determine the thickness of the dead layer in each pixel, data with two alpha and one electron sources were taken.

Acknowledgements

Dirk and Pico, without your intriguing lectures in the nuclear physics course, I would never have thought of following the “Nuclear World”. Dirk, thank you for reading my drafts and for always checking that everything was on track. Danny, Fusion 360 would have been a nightmare without you and your knowledge. Pavel, thank you for explaining to me how the detectors work. Pico, from the Data Acquisition System, to the C++ code, to your method of explaining complicated topics in an easy way... I cannot thank you enough. Tanvir, without you and the countless fikas together, this wouldn't have been so much fun. Yuliia and Dalia, you have been a great company. This semester has been a blast and I thank all of you for this. I would also want to thank my family for always supporting me in every step and for always believing in me.

Contents

1	Introduction	4
2	Theory	5
2.1	Passage of radiation through matter	5
2.1.1	Alpha particles	5
2.1.2	Other heavy ions	6
2.1.3	Electrons	6
2.2	Silicon detectors	7
2.2.1	Plasma effect	9
2.3	LUNDIUM	9
2.4	Dead layer of silicon detectors	10
3	Method	12
3.1	Experimental setup and data acquisition system	12
3.2	Data Analysis	15
3.3	Calibration of the DSSSD	15
3.4	Dead layer determination	15
4	Results	17
5	Discussion	21
6	Conclusion & Outlook	21
A	Appendix	23
A.1	Fusion 360 [©]	23
A.2	Mapping	24

1 Introduction

Atoms are the smallest units of common matter, consisting of electrons, protons, and neutrons. Protons and neutrons are concentrated in the atomic nucleus and are held together by the nuclear force. Probing into the nucleus, the number of protons, Z , which is equal to the number of electrons, determines the chemical properties of the atom. A chemical element is a pure substance containing atoms that have the same Z number. Each of the chemical elements has different isotopes, which are determined by the number of neutrons, N . All these pairs of known proton and neutron numbers are combined in the “Chart of Nuclides”, which includes all the known atomic nuclei so far. The “Chart of Nuclides” can be seen in Figure 1.

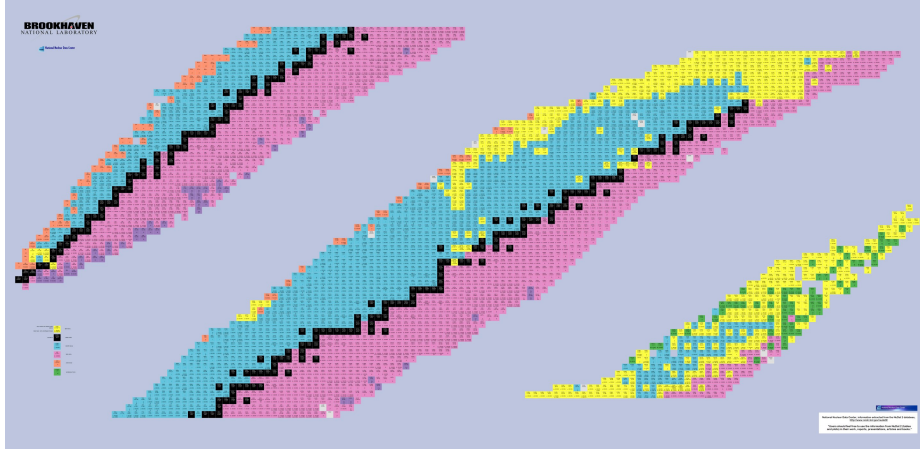


Figure 1: A Chart of Nuclides, which is cut in three parts for a better demonstration [1].

Stable nuclei, which are marked as black in the figure above, remain unchanged over time, whereas unstable nuclei are radioactive. When unstable nuclei decay, they emit different types of ionizing radiation such as α , β , and γ particles. Nuclear physics deals with the understanding of the atomic nucleus as well as the radiation emitted from the unstable nuclei.

A very active field of nuclear physics deals with the uppermost part of the Chart of Nuclides, focusing on superheavy elements or transactinides, whose number of protons is greater than 103. Observing the line of stability, at low mass number A , stable nuclei lie close to the middle of the chart where $N=Z$. What is intriguing about superheavy elements is that the number N is much greater than Z . These exotic nuclei are all artificial, that we know of, and with a very short half-life. Because they are created synthetically in the laboratory, they can only be studied by the detection of their decay products. To detect the radiation emitted, high quality detectors are used – detectors of first-rate – to make sure that as much as possible of the radiation emitted from them is recorded.

The LUNDIUM decay station, to be the worlds best decay station, is currently being built in Lund. It includes new instruments that boost the sensitivity of decay-spectroscopy studies. It involves high-purity germanium detectors for detecting photons and silicon detectors responsible for the detection of charged particles. There are in total six silicon detectors: one implantation detector, one veto detector, and the remaining four are called box detectors. The implantation detector and the box detectors are arranged in a cubic-shape with one side left open for the nuclei of interest to enter. The sixth silicon detector, the “veto detector” is placed right behind the implantation detector. It is responsible for detecting β decay electrons that escape the implantation detector. Just behind each silicon detector, Compex detectors are placed, for photon detection. Compex detectors are unique since they are the first detectors worldwide composed by four coaxial, cubic-shaped, encapsulated germanium crystals. The use of Compex detectors will improve the energy resolution and will be capable of detecting low-energy photons [2].

This thesis focuses on characterizing the implantation detector, in particular, determining its pixel-by-pixel dead layer thicknesses. The implantation detector is placed in front of the radiation source. Hence it will play a significant role in recording the energies of the incoming particles. When it comes to decay spectroscopy, one should be very precise with the recorded energies. Even a small offset of the full energy detected from the original deposited energy can result in misleading results. When measuring the energy of charged particles with silicon detectors using an external source, one always notices a recorded energy smaller than the expected one. This is due to the dead layer surface of silicon detectors, which is unable to record the energy deposited from the particles in the dead layer region. However, one is able to reconstruct the full energy of the particles by knowing the thickness of the dead layer. In this thesis, I measure the thickness of the dead layer by measuring the energy loss of α particles by irradiating the detector from different distances. Furthermore measurements with an electron source were taken, which were used for calibrating the detector.

2 Theory

2.1 Passage of radiation through matter

Ionizing radiation normally consists of highly energetic particles. Its interaction with matter predominates in the experimental work and the applications of nuclear physics. In order to detect a particle, it must interact with the material of the detector and transfer energy which is further analyzed by the electronics. Charged particles interacting with matter lose energy as a result of two processes; elastic scattering from nuclei and inelastic collisions with the atomic electrons. Because the nuclei occupy only a tiny fraction of the atoms inside the material, it is more likely for the particles to collide with electrons than with a nucleus. This is why the governing mechanism of energy loss by charged particles is Coulomb scattering by atomic electrons.

2.1.1 Alpha particles

All the radioactive nuclei, whether they occur naturally or are synthesized in the laboratory, can emit a combination of α , β , or γ radiation. Radiation produced by the radioactive nuclei that exist in the environment, together with cosmic rays coming from the outer space that hit the surface of the earth every single second, give rise to the background radiation that we are all subjected to. Since its unknown when unstable nuclei will exactly decay, their half life can be determined, which is the time it takes for half of the nuclei to decay. The α sources used for this experiment have half-lives of 18 and 74 years.

As can be seen in Figure 1, α decay (yellow) happens usually in the upper left of the chart. This is a region for which the neutron to proton ratio is too small. When there are a lot of protons inside the nucleus, the Coulomb force overcomes the nuclear force, which is responsible for keeping the nucleons together. The α particle which is emitted has two protons and two neutrons, ${}^4_2\text{He}_2$, which results in a more stable decay product. ${}^4_2\text{He}_2$ has a very stable and tightly bound structure since it consists of a nucleus with doubly magic numbers. It can be emitted spontaneously in α decay if the Q-value of the system is positive. Alpha decay is described by the following equation:

$${}^A_Z\text{X}_N \longrightarrow {}^{A-4}_{Z-2}\text{X}'_{N-2} + {}^4_2\text{He}_2. \quad (1)$$

The inelastic collisions between the charged particles and the atomic electrons are statistical in nature and they take place with a certain probability. However, since the fluctuations over the path are small over a short period, one can simplify the equations and work with the average energy loss per unit path length [3]. The rate at which a heavy charged particle loses energy per unit length is known as the stopping power. Consider a particle with electron charge e , atomic number z , travelling at relativistic speed v . The Bethe & Bloch formula is then given by:

$$-\left\langle \frac{dE}{dx} \right\rangle = \left(\frac{e^2}{4\pi\epsilon_0} \right)^2 \cdot \frac{4\pi}{m_e c^2} \cdot \frac{n z^2}{\beta^2} \cdot \left[\ln \left(\frac{2m_e c^2 \beta^2}{I(1 - \beta^2)} \right) - \beta^2 \right], \quad (2)$$

where ϵ_0 is the vacuum permittivity, m_e is the mass of an electron, $\beta = \frac{v}{c}$ and c is the speed of light in vacuum. The quantity I is the mean energy required to ionize an atom in the medium and for practical purposes is approximately equal to $I = 11 \cdot Z$ eV [4].

The target material has an electron density n that is calculated by the following equation:

$$n = \frac{N_A \cdot Z_t \cdot \rho}{A_r \cdot M_u}, \quad (3)$$

where N_A is the Avogadro constant, Z_t is the proton number of the target material, ρ is the density of the target material, A_r is the atomic weight and M_u is the molar mass constant.

Due to their comparably large mass, α particles follow an almost straight line even though many collisions with electrons take place. Given a particle with energy, E , the calculation of the mean range of a particle is obtained by integrating the inverse of the stopping power as seen below:

$$R = - \int_{E_f}^{E_i} \left(\frac{dE}{dx} \right)^{-1} dE. \quad (4)$$

2.1.2 Other heavy ions

Knowing the stopping power is a matter of importance when one wants to reconstruct the energy of a particle. In the early years, before the stopping power for a lot of the nuclei was known, Segré came up with scaling laws for the Bethe-Bloch formula. More specifically, if the material medium is uniform, the particles passing through will lose an amount of energy per unit length that is only dependent on the particles velocity and charge. The equation describing this is the following:

$$-\left\langle \frac{dE}{dx} \right\rangle = z^2 f(\beta), \quad (5)$$

where $f(\beta)$ is dependent only on the velocity [3].

By expanding the previous equation, it can be seen that if the charge and the velocity of two different particles is known, then the stopping power in the same material can be calculated by a scaling factor:

$$-\left\langle \frac{dE_2}{dx}(T_2) \right\rangle = -\frac{z_2^2}{z_1^2} \frac{dE_1}{dx} \left(T_2 \frac{M_1}{M_2} \right), \quad (6)$$

where T_2 is the kinetic energy of the second particle, z_1 and z_2 are the charges and M_1 , M_2 are the masses respectively [3].

2.1.3 Electrons

The Bethe-Bloch formula is modified for the electrons due to two reasons. To begin with, electrons have a much lower mass compared to heavy ions. Hence, during the collisions, the assumption that the incident particle remains undeflected is invalid. When dealing with electrons, one has to take into account the bremsstrahlung radiation which is caused due to sudden deflection of the particle. Furthermore, the collisions for electrons are between identical particles. Therefore, one should take into account their indistinguishability. The Bethe-Bloch formula for electrons is then described by the following equation, where r is the subscript for the energy loss due to radiation, and c stands for the energy loss due to collisions.

$$-\left\langle \frac{dE}{dx} \right\rangle = \left\langle \frac{dE}{dx} \right\rangle_c + \left\langle \frac{dE}{dx} \right\rangle_r. \quad (7)$$

2.2 Silicon detectors

In a crystal lattice, the atoms have a periodic arrangement with valence electrons participating in covalent bonding. As known from the atomic structure, electrons have quantized energy levels and can occupy different states. At absolute zero, i.e., 0 K, the last occupied state that the electrons can reside in is the valence band. The first unoccupied state is called the conduction band. In a semiconductor, these states are separated by a potential difference of approximately 1 eV, which is called the band gap. This difference is caused by the overlap of the electron wave functions; Pauli exclusion principle forbids two electrons from having the same quantum numbers. Hence, in higher atomic shells, the degenerate states break into separate states that have a small distance between them.

Semiconductors differ from insulators and metals on the size of the band gap. At room temperature, in a semiconductor, few of the electrons might gain enough energy to jump to the conduction band leaving a hole in the valence band, which acts as a positive charge carrier. This will create some conductivity, as a result of the electrons moving in the conduction band and the holes in the valence band. However, it is low compared to a conductor. On the contrary, inside a conductor there is no band gap and electrons can easily move into the conduction band where they are less bound to the ions forming the crystal. Furthermore, in an insulator, the band gap is on the order of 5 eV, making it in practice impossible for electrons at room temperature to gain enough energy and overcome the gap. The difference of the band gaps is shown in Figure 2 below.

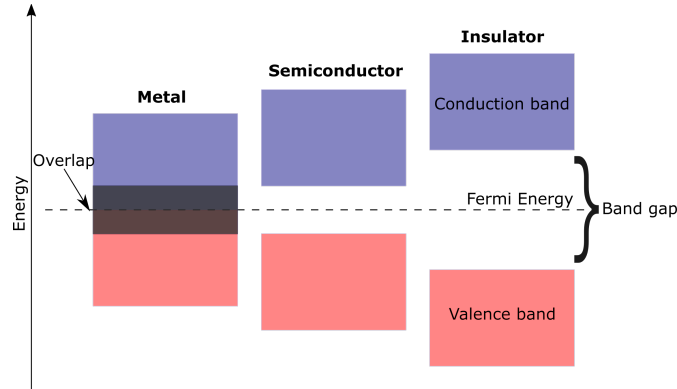


Figure 2: A band gap schematical diagram showing the differences of the band gaps for metals, semiconductors, and insulators. The Fermi energy lies in the middle of the band gap, and it is used to describe the top of the collection of electron energy levels at absolute zero temperature.

Semiconductor materials are usually made out of silicon and germanium since they are tetravalent, meaning that they have four valence electrons in the outermost shell. In this case, the semiconductor is called “intrinsic” since it is a pure element. When doping a semiconductor by adding impurities, extra energy levels appear, which increase the conductivity of the material. By adding an impurity that has three valence electrons, one dopes the semiconductor and this is called p-doping. If one adds an impurity atom of five valence electrons, the doping is called n-doping. This is then referred to as extrinsic semiconductor. An illustration of the electronic band structure of an n- and p-type semiconductor is shown in Figure 3. During n-doping, the band structure of the crystal is perturbed and an extra donor state is added close to the conduction band. For p-doping, the additional state is created very close to the valence band, as can be seen in Figure 3. The procedure of ‘giving’ electrons to the conduction band and ‘taking’ electrons from the valence band, that is generating holes, strongly influences the conductivity of the semiconductor.

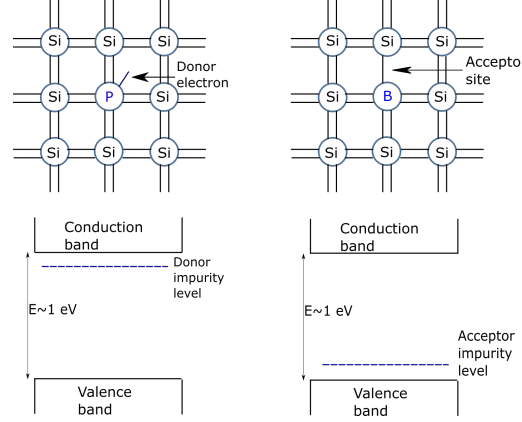


Figure 3: Illustration of donor and acceptor states when doping a semiconductor.

When n- and p-doped materials are joined together, a p-n junction is formed. In this way, charge carriers are free to migrate across the junction. More specifically, electrons diffuse towards the p-side and holes diffuse into the n-side. The recombination of electrons and holes will create a region, called the depletion zone, with no free charge carriers, since the number of electrons matches the number of holes. The ionized atoms then give rise to an electric field. The electric field is proportional to the width of the depletion zone. When there is no external bias applied to the p-n junction, there exist drift and diffusion currents which are equal in magnitude and opposite in direction. Hence the net current is zero. The current across the junction can be carried by both electrons and holes and these are often discussed together as charge carriers. The total conductivity in the semiconductor is given by the formula:

$$\sigma = e(n\mu_e + p\mu_h), \quad (8)$$

with n and p representing the electron and hole densities, and μ_e and μ_h their mobilities, respectively. The current created when no bias is applied to the system is too small for the semiconductor to function as a detector. Furthermore, electrons in the n-side and holes in the p-side cannot overcome the barrier. In order to increase the detector response of the device, a bias is applied over the junction. By connecting the positive end of the circuit to the p-side and the negative end to the n-side, a forward bias is added to the system. In this case, the voltage across the depletion region drops, making the conductivity of the majority carriers through the semiconductor to increase. This will result in the current to increase exponentially. When the p-n junction is formed, electrons that move to the p-side will generate a drift current which is due to the electric field dragging them to the n-side. This current remains unchanged even when external voltage is applied to the system. On the other hand, the diffusion current, which is the current generated by the majority electrons on the n-side that due to their high energy can overcome the electric field in the depletion region and migrate to the p-side, changes with regard the applied external voltage. Equation 9 shows the differences of these voltages; forward bias leads to exponential increase of the voltage, whereas reverse bias results in a current that is quite small [5].

$$I = I_{diffusion} - I_{drift} = \begin{cases} I_0(e^{-eV/k_B T} - 1), & \text{reverse bias} \\ I_0(e^{eV/k_B T} - 1), & \text{forward bias.} \end{cases} \quad (9)$$

The depletion zone is the part of the detector that is sensitive to radiation. Under the influence of an external electric field, electron-hole pairs form a current pulse, which is the signal processed by the electronics. In principle, the ionizing particles entering the detector produce electron-hole pairs that we get the pulses from. Electrons will drift towards the n-side of the detector and holes towards the p-side and the current pulses will then be proportional to the energy deposit. The change of the band gap when a reverse bias is applied can be seen in Figure 4.

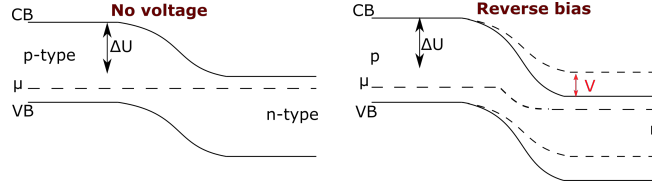


Figure 4: The variation of the electric potential across the band gap when there is no external voltage applied to the system (left) and when a reversed bias is applied (right).

Since one is interested in measuring the energy of the incident radiation entering the detector, energy resolution is the most important feature for the detector. The energy resolution in a semiconductor detector depends on the primary number of the electron-hole pairs that were formed. The variance on the number of charges and the resolution, which is expressed as “full width at half maximum” (FWHM), are given by:

$$\sigma^2 = FJ, \quad (10)$$

$$R = 2.35\sqrt{\frac{F}{J}} = 2.35\sqrt{\frac{Fw}{E}},$$

where J is the mean ionization and F is the Fano factor. For semiconductor detectors the Fano factor is in the order of 0.12. In the resolution equation, w is the average energy for an electron-hole pair creation and $J = E/w$. The Fano factor is an empirical factor and is equal to 1 when the fluctuations on the number of the formation of the electron-hole pairs can be described by a Poisson distribution. In case of semiconductor detectors, the Fano factor is less than one because the energy conservation that the total energy of the pairs created should be equal to the energy of the incoming α particle, reduces the fluctuations on the number of the pairs produced [3].

2.2.1 Plasma effect

When doing heavy-ion spectroscopy, of particular interest is the plasma effect. Since a lot of electron-hole pairs are created, a dense cloud of them is produced which affects the pulse height of the resulting signal. The electric field that is created by the applied voltage is locally nullified. This will cause a delay in collecting the charge since the risetime of the pulse is much slower when the electric field is weaker, which is called the plasma time. Furthermore, in semiconductor detectors, it is important to avoid the recombination of the electron-hole pairs, after the ionizing radiation has entered the detector. However, during the delay, some of the electron-hole pairs might recombine. Hence, the collected charge will be less than what was originally created. This results in a degradation of the energy resolution [3].

2.3 LUNDIUM

The LUNDIUM decay station is currently being built in Lund by the Nuclear Structure Group, and it will play a significant role in answering questions about the next proton magic number (we already know that $Z=114$ is not a magic number [2]) and the “Island of Stability”. By discovering the heaviest elements that can exist in nature, questions about the nuclear structure can be given as well. What is world-unique about LUNDIUM are the new Compex germanium detectors. Due to their efficiency, one will be able to measure the Z -fingerprint of the superheavy elements and the K & L x-rays coincidences. A 3D render of the decay station made in Fusion-360 is shown in Figure 5. The implantation detector and the four box detectors, which have 32 strips on each side and are $500 \mu\text{m}$, are positioned in a cubic shape. The veto detector, is placed just behind the implantation detector. It is used for vetoing, in order to get a better selection of events of interest [6]. The five Compex detectors are placed behind each of the silicon detectors. A Compex detector is made of four $5 \times 5 \times 5 \text{ cm}^3$ germanium crystals in a clover array. The close structure increases the solid-angle coverage and thus the efficiency for detecting photons [2]. Further improvements are

made by reducing the background in the Compex detectors. This is achieved by adding BGO anti-Compton suppression shields around them. BGOs act as a veto for γ rays that escape from the Compex germanium crystals [7]. The whole system will operate in vacuum. This is due to the Compex germanium detectors. These detectors, besides having cubic crystals, are designed to be operated without their end caps inside LUNDIUM. This will increase the lifetime of the detectors as well as it will boost their sensitivity.

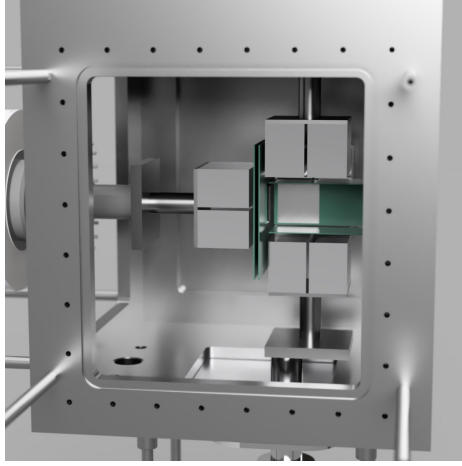


Figure 5: A 3D render of LUNDIUM. One can notice the silicon detectors (green) and the Compex Germanium crystals surrounding them. Notice the end cap of the Compex detectors is removed.

2.4 Dead layer of silicon detectors

The implantation DSSSD has 58 strips on the p-side and 58 strips on the n-side; p- and n-side strips are perpendicular to each other creating a two-dimensional space with a grid of 3364 pixels. The p-side of the detector is directed towards the inside of the silicon cube. Hence, all the α particles which reach the detector will lose energy in the dead layer of the p-side. In this thesis the dead layer of the p-side is determined which is of high interest for charged particles who escape the implantation detector and are stopped in one of the box detectors positioned upstream [8]. For determining the n-side dead layer thickness, one would have to irradiate the n-side of the detector respectively.

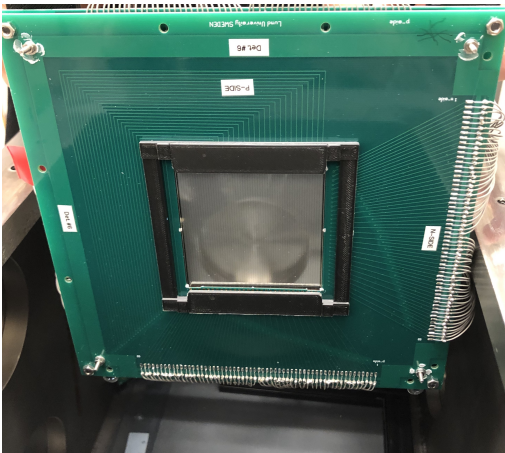


Figure 6: The implantation detector used in this experiment.

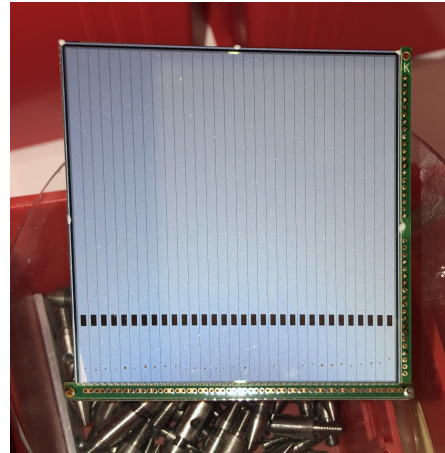


Figure 7: A LYCCA silicon strip detector, where the strips are more clearly visible.

For charged-particle detection, silicon semiconductor materials are used. They are suitable for measuring the energy loss and the position (if the detector is “pixelated”) of the charged particles. The dead layer is a characteristic of the silicon detectors and its thickness should always be taken into account when someone wants to achieve the best performance from them. The DSSSD used in this experiment has a homogeneous, square shape ($60.1 \text{ mm} \times 60.1 \text{ mm}$), n-doped silicon wafer which is approximately $320 \text{ }\mu\text{m}$ thick. The active area of the detector is $58.5 \text{ mm} \times 58.5 \text{ mm}$ and there are a 58 strips on each side [9]. Dividing the thickness of the active area by the number the strips, the pitch of the detector is found. In our case the pitch is very close to 1 mm .

In order to achieve a semiconductor junction, p+ type impurities (Boron) are implanted into the wafer using an accelerator. Using the ion-implanted method, the surface becomes heavily doped, which results in a relatively thick dead layer of the material. This region then becomes unable to record the energy deposited by charged particles, hence there is an energy loss in the final energy measurement. In the same way, a n+ type impurity (Arsenic) is implanted on the opposite side of the detector. A layer of aluminium is added for better conductivity. Lastly, since silicon oxidizes at room temperature, a further layer of silicon dioxide SiO_2 is added on the top, making the wafer silicondioxide passivated [3]. The composition of implanted ions, silicon dioxide, and aluminium which serves as an electrical contact, produces the total dead layer, the thickness of which will be determined in this thesis. The dead layer over the detector is likely to be not uniform, so the dead layer thickness of each pixel is to be determined. The method for determining the thickness for the dead layer as well as additional information about it are discussed later in Section 3.

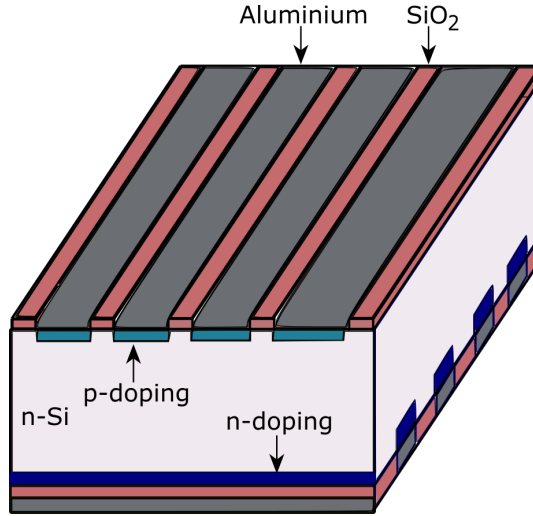


Figure 8: Schematic showing a DSSSD and the dead layer composed of p- and n-doping, aluminum and SiO_2 . By reading the electron-hole pairs generated in the perpendicular grid, it is possible to determine the x-y position of the interaction.

3 Method

3.1 Experimental setup and data acquisition system

The experimental setup inside the vacuum chamber for determining the dead layer is shown in Figure 9. A ruler was placed inside the chamber to measure the position of the detector and the position of the source. The wires that can be seen in Figure 9, connect the Printed Circuit Boards, PCBs, to the preamplifiers.

When measuring the dead layer of the detector, one has to be very careful with the distances between the radioactive source and the detector. This is because the thickness of dead layer that the particles pass through, is heavily dependent on the incident angle with respect to the surface of the detector. If the source is far away, the angle of incidence is close to zero (perpendicular to the detector surface) and the particles reaching the detector will travel through the minimum amount of dead layer. Particles coming from a source which is closer to the detector, come at a shallower angle towards the edge of the detector and travel through a thicker dead layer. For this thesis, data with different sources and also different distances between the source and the implantation detector were taken.

A summary of the main experimental parameters for this thesis, can be seen in Table 1. A ^{148}Gd source was used for taking data at two different distances. For our first measurement, the source and the detector were about 8.4 cm apart. We also aimed that the source was roughly aligned with the center of the detector. For our second measurement, the source was placed about 3.1 cm away from the detector. Details for the other sources, as well as the emission energies of every source are given in the table below.

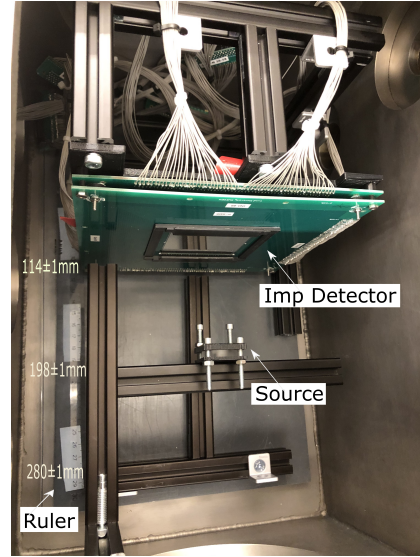


Figure 9: Picture from inside the chamber showing the distance between the source and the detector for the first measurement with ^{148}Gd .

Lab Measurements				
Source	Bismuth-207(e^-)	Barium-133(e^-)	Gadolinium-148(α)	Curium-244(α)
Distance (cm)	8.4(1)	8.4(1)	8.4(1) & 3.1(1)	8.4(1)
Energy (keV)	480.5(1)	320.03(1)	3182.7(1)	5804.8(1)(76.9%) & 5762.6(1)(23.10%)

Table 1: The experimental parameters used in this thesis.

Given that the implantation detector was used for the very first time for this work, we made sure that all the electronic channels were working. This was done by connecting the preamplifier output to an oscilloscope channel by channel as can be seen in Appendix Figure 39.

The experiment was carried out at the Nuclear Structure Group laboratory here in Lund. In Figure 10, taken at the lab, the main four components used for the experiment are shown: the vacuum chamber, the FEBEX crate, the readout PC and the NIM crate. The vacuum pump and the control PC are not visible. However, all the different components used in this experiment are listed in Figure 11 and their descriptions are given below.

The 58+58 signals from the implantation detector (58 from the p-side and 58 from the n-side) were connected to four IKP Cologne-built preamplifiers. The preamplifiers were cabled as close as possible to the detector, in order to minimize the possibility to pick-up noise and each one of them processed up to 32-channels. Following, the signals were connected to eight 50 MHz sampling, ADC FEBEX3 digitizer cards, with 16 inputs each. The first four cards read signals from the p-side of the detector; 0 and 1 were connected to strips 0-15 and 16-32 respectively, and 2 and 3 were connected to strips 33-47 and 48-64. In the same way, FEBEX cards 4-7 were connected to the n-side of the detector. Since we had 58 strips and 64 cables, some channels had no inputs. A reverse -40 V bias was applied from the MESYTEC MHV-4 module to the detector. Lastly, since one wants to avoid the interaction of the particles with air, the chamber was evacuated, which was monitored by a digital vacuum gauge. The reverse bias was applied once the system was in vacuum.

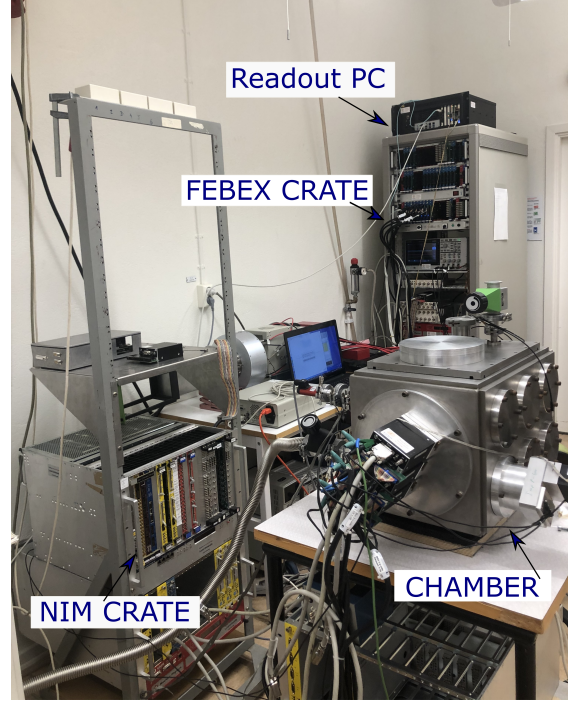


Figure 10: Figure taken at the lab that shows the main components of the experimental set-up.

When a particle triggered the system above a certain threshold on the p-side, the pulse height observed in the preamplifiers which is proportional to the deposited energy, was recorded. This pulse was digitized by the FEBEX3 cards and it was further sent to the Readout PC, where the MBS (multi-branch system) [10] data-acquisition system (DAQ) was running. In the Control PC, the traces were seen using Go4 [11], which is based on ROOT [12]. Before recording data, the traces were monitored and were assessed, making sure that the data acquisition was correctly set and that the system was noise-free as much as possible. The data analysis is discussed in Section 3.2.

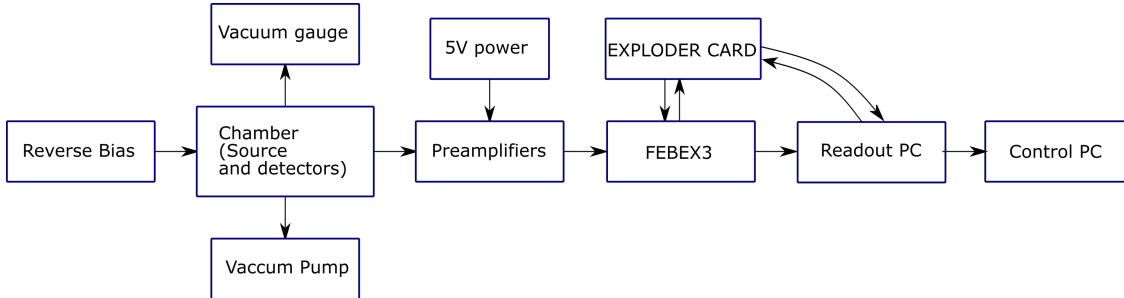


Figure 11: A diagram showing schematically the components of the DAQ and the experimental setup.

The preamplifiers used in this experiment are charge sensitive. They are used together with radiation detectors, due to their high capacitance. Because the voltage pulse that is obtained in the preamplifier is small, it is important that the capacitance of the system remains stable over time. This is achieved by assuring that the capacitance of the preamplifiers is much larger than the input capacitance (detector, cables etc). For this experiment, four similar preamplifiers were used and can be seen in Figure 12. They have been designed and manufactured at IKP Cologne, and they have two possible gains, $\times 1$ and $\times 3$, such that the linear dynamic range can be 15 MeV or 45 MeV respectively. A MESYTEC MNV-4 module located in the NIM crate is responsible for powering the preamplifiers. A 5 V power was applied to them. For minimizing the noise, the four preamplifiers were grounded together, which lead in smaller ground loops.

The way that the preamplifiers were connected to the FEBEX cards is of the essence when we map the p- and n-sides of the detector to the real x and y coordinates. Before starting with the actual data analysis, a nonsymmetric paper mask was placed in front of the detector to stop the α particles. The 2D hit pattern and the shadow of the paper, showed whether the mapping was done correctly. See Appendix A.2.



Figure 12: Picture of a preamplifier used in this experiment.



Figure 13: The Febex crate used in the experiment.

The FEBEX crate was connected to the EXPLORDER card through a clock and deadtime locking cable. The EXPLORDER card was responsible for handling the trigger of the system and the clock synchronization of the digitizers [13]. When the detection rate is very high, the exploder card stop accepting signals, in order for the pulses to not overlap. This gives the possibility for the system to detect smaller pulses which might be of great interest. Inside the FEBEX3 cards, the ADC (Analog to Digital converter) and the FPGA (Field Programmable Gate Array) were located. An algorithm running in the FPGA delivered the time and the energy to the Readout PC through a fibre-optic cable and subsequently to the Control PC, where they were further analyzed using the Go4 analysis framework.

3.2 Data Analysis

The data analysis was performed using Go4. Go4 stands for GSI Object Oriented On-line Offline and is an analysis framework developed at GSI, based on ROOT [11]. The data processing followed three steps; unpacking, mapping and analysis. From the experiment, the raw data that one gets from the MBS data acquisition system are binary List-Mode Data files (LMD). The first step, called unpacking, involved the mapping of the binary contents into C++ data structures [2]. More specifically, the binary file that had the raw data in a LMD format, was unpacked and the data were stored in a ROOT-tree. During the mapping step, the unpacked data were mapped into the p- and n-side of the detector. The mapping step also involved the translation of the p- and n-coordinated to the real x- and y-positions. The mapping process was done by comparing the energies in the p- and n-side of the detector. If the energy in one of the p-strips was very close to that of the n-strip and if the time between these two events was very close, then a pixel was considered to be formed, which gave the p and n position of the particle that hit the detector. Since the number of strips in the detector is known, and the distance between each strip is given, the p- and n-sides were easily transformed to the real two-dimensional space. The last step was the data analysis, which is explained below.

3.3 Calibration of the DSSSD

An energy calibration was done at the beginning of the experiment. An electron source and the two α sources (^{148}Gd and ^{244}Cm at a distance of 8.4 cm for both) were used for the calibration. First, for the low energy point, a ^{207}Bi electron source was used. In general 100 keV electrons pass through $\sim 100 \mu\text{m}$ of detector material. Since the detector used in this experiment is in the range of $320 \mu\text{m}$ thick, the electron source that emits electrons in the energy range of at most 320 keV should be chosen. Finally, the electron source ^{133}Ba was chosen. This was done to relate the recorded FPGA pulse height to energy. For each strip of the detector, three peaks were fitted. A Gnuplot scrip was used to fit the Gaussian curves [17].

3.4 Dead layer determination

In our experiment, the source was naturally positioned outside of the detector hence all the particles recorded deposited energy in the dead layer. This is different from some in-beam conditions where the source is implanted inside the detector. The energy loss of the α particle in the dead layer region when the angle of incidence is zero, and when the angle of incidence is θ is given by the following equations:

$$\begin{aligned}\Delta E_0 &= \frac{dE_0}{dx} \cdot t, \\ \Delta E(\theta) &= \frac{\Delta E_0}{\cos\theta},\end{aligned}\tag{11}$$

where t is the thickness of the dead layer [14].

The difference of the energy for measurements taken with an incident angle of 0 and θ is described by the equation:

$$E' = \Delta E_0 \left(\frac{1}{\cos\theta} - 1 \right).\tag{12}$$

The traversed length that the particles will follow, is related to the dead layer by a “geometrical factor” and it has a different value for every pixel.

To determine the dead layer of the implantation detector, a Jupyter notebook written originally for TASISpec by Anton S  mark-Roth [2] was reworked. Calculated peak positions after dead layer for each pixel were used for the different sources and they were compared to the experimentally obtained peak positions. A possible difference in energy was attributed to the thickness of the dead layer. Any offset in the difference was due to the geometrical factor which was also taken into consideration.

The energy loss $\frac{dE}{dx}$ as a function of the energy of the incoming α particle was calculated using pySRIM [15], which is based on SRIM [16]. As mentioned before, the dead layer is a mixture of aluminium, SiO_2 and implanted ions. However, the biggest impact is from the SiO_2 and for simplicity the entire dead layer was assumed to be SiO_2 . For the calculated data with pySRIM, interpolated values were added, since the stopping power obtained from SRIM was very discretized.

In a superheavy element spectroscopy experiment, from a fusion-evaporation reaction, the evaporation residues (EVR) are implanted into the implantation detector. The energy of the EVR should be high enough to make sure that it will be implanted after it has passed the dead layer of the detector. In this case, the particles emitted during radioactive decays, can either travel into the remaining part of the implantation detector without going through the dead layer or they can escape from the implantation detector and go into one of the box detectors. In the last case, when reconstructing the energy of the α particle, one has to take into account the pixel dead layer of both the implantation and the box detector [2].

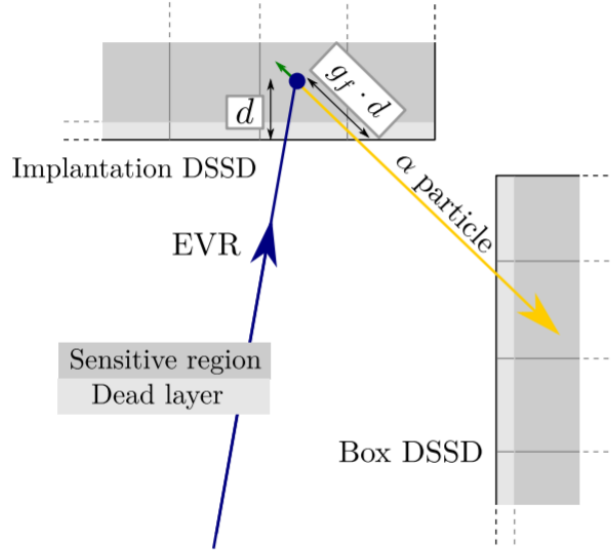


Figure 14: Two-dimensional representation of a typical escaping α decay following an EVR implantation. The geometrical factor (perceived increased in thickness of the dead layer due to the angle of incidence) in both dead layers is taken into account when the α particle escapes from the implantation detector [2].

4 Results

The scope of this thesis was to calculate the thickness of the dead layer over the entire implantation detector surface. To achieve this, a sequence of work had to be done. To begin with, since the dead layer was expected to not be uniform over the detector, the mapping step during the Data Analysis was crucial for knowing the exact x- and y-position of the interaction.

Before mapping the data in x- and y-positions, the number of counts was shown in p- and n-side coordinates. Subsequently the 2D hit pattern in real space of the detector could be visualised as well. The plots below show the 2D hit pattern of the ^{148}Gd source when it was positioned close to the detector (3.1 cm). As mentioned before, the angle of incident influences the amount of dead layer that the particles will pass through. When arranging the x, y and z position of the source before the experiment, we tried to align the middle of the source with the middle of the detector. The y position of the source was around 5 mm lower than that of the center of the detector, which can be seen in Figure 16, where the hit pattern is mapped in the real x- and y- coordinates.

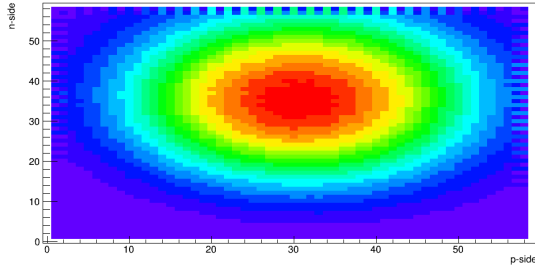


Figure 15: 2D hit pattern in p- and n-side space for the implantation detector using the ^{148}Gd source at close distance.

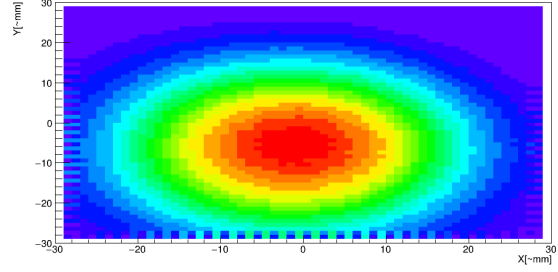


Figure 16: Same as Figure 15 but mapped in x- and y-coordinates.

In Figure 15, one notices that the source is shown to be positioned higher than the middle of the detector. This is because the orientation of the implantation detector is rotated 180° and the channel numbers are read as shown below:

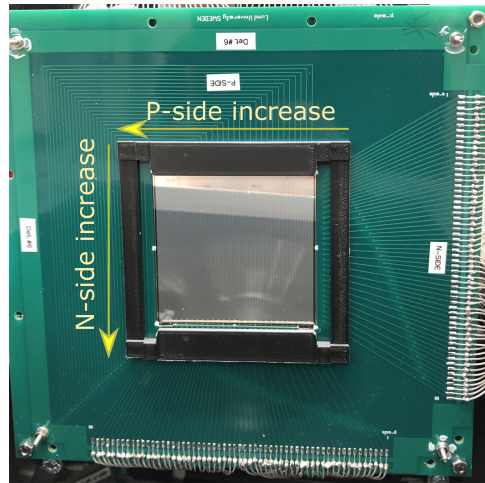


Figure 17: Orientation of the implantation detector. The first channel for both sides is read in the upper right side of the detector. The p-side grows from right to left and the n-side from above to below.

The previous plots were the final plots that we got from the data analysis step. For those plots to be produced, the mapping had to be done as well as creating the pixels. For details of mapping see Appendix A.2.

The process of calibrating in energy the detector was done by using a Gnuplot script [17]. The calibration was done for every strip of the detector and three peaks per strip were fitted. The Figures below show the uncalibrated and calibrated strip data for ^{148}Gd source, positioned 8.4 cm away from the detector.

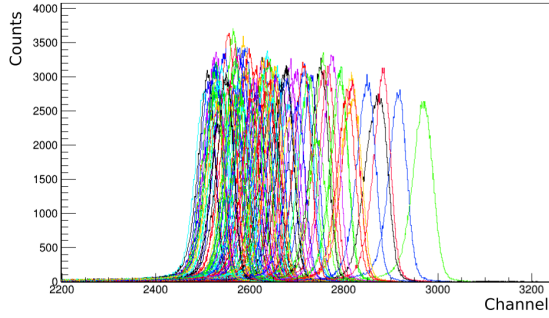


Figure 18: Uncalibrated strip data for ^{148}Gd source positioned 8.4 cm away from the detector.

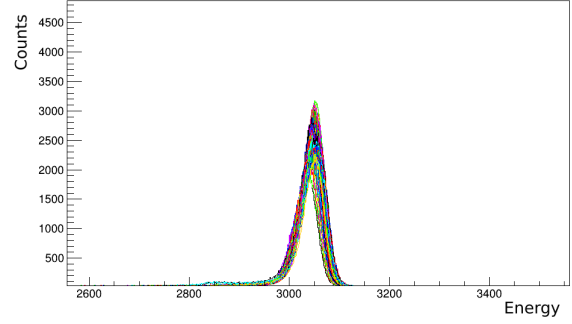


Figure 19: Same as Figure 18 but energy calibrated.

Also, the uncalibrated and calibrated spectra of ^{244}Cm are shown below. The α particles emitted from this source have energies of 5805 keV with an intensity of 76.9% and 5763 keV with an intensity of 23.10% respectively. In the calibrated data, Figure 21, one can notice the two peaks.

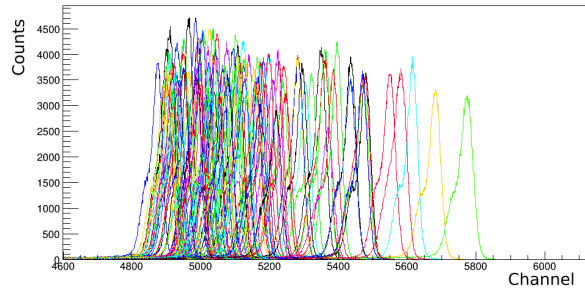


Figure 20: Uncalibrated strip data for ^{244}Cm source.

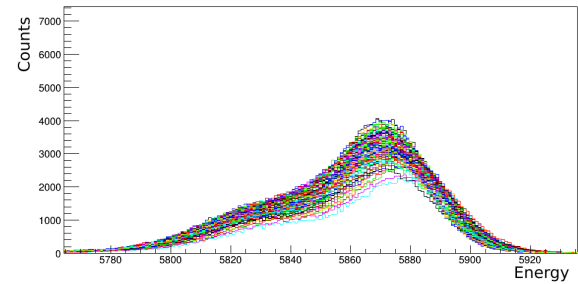


Figure 21: Calibrated strip data for ^{244}Cm .

Of great interest is the calibration of the ^{148}Gd source when it was positioned very close to the detector. This measurement highlights the importance of the incident angle and the energy loss of the particles in the dead layer region. This can be easily visualised in the Figures 22 and 23. Figure 23 shows the distributions of energies per strip number. Strips 1-58 represent the p-side and 59-126 the n-side. After calibrating the detector, one expects an energy distribution that resembles a straight line at the energy of the particle. However, as can be seen the dead layer plays a significant role in the energy recorded.

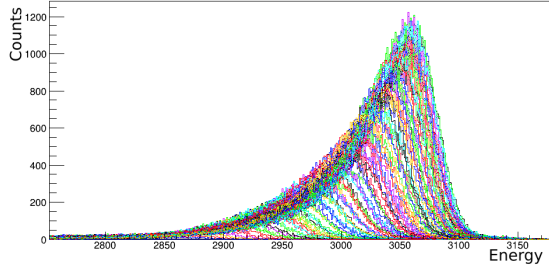


Figure 22: Calibrated spectrum for ^{148}Gd , close distance. The fact that there is not a single perfect peak demonstrates that the dead layer heavily affects the energy measurements.

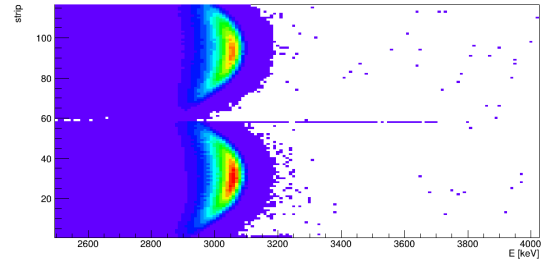


Figure 23: Experimental energy distribution per strip number for the implantation detector using a ^{148}Gd source, positioned at a distance 3.1 cm from the detector.

The dead layer is determined for each pixel of the detector. For a pixel to be formed, the energies in the p- and n-side must within a small range. The straight line in Figure 25 represents the formed events filtered to be suitable to be used as pixels. If the p- and n-side registered the same energy, we can be more certain that correspond to the correct detection of a particle.

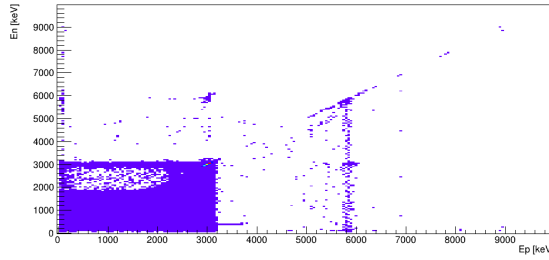


Figure 24: Experimental distribution of energy for both sides (p vs n) of the detector.

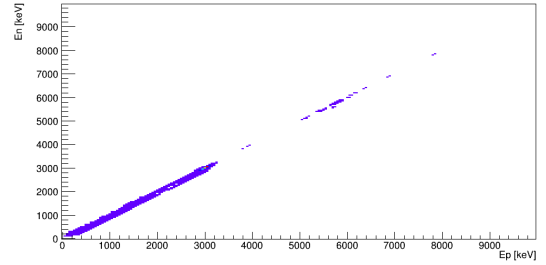


Figure 25: Experimental distribution of energy for both sides (p vs n) of the detector, after setting the condition that the energies of both sides should be equal.

In a similar way, for a pixel to be formed, the time of the hits in the p- and n-side should be very close, ideally the same as well. Below, the time recorded from the FPGA is plotted for the n-strip vs the p-strip. The vertical and horizontal lines represent the trigger time, which is set to 285 channels of 20 ns each corresponding to our 50 MHz sampling rate. The spikes and the diagonal line show the hits from the particles. In Figure 27, the time for both sides is set to be close within $1\ \mu\text{s}$ and only the pixels fulfilling this conditions are shown.

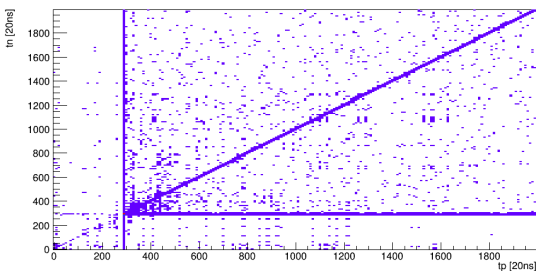


Figure 26: Time distribution over the p- and n-side of the detector.

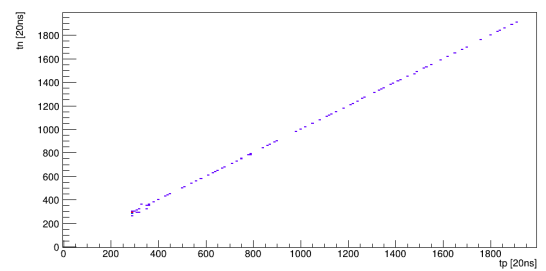


Figure 27: Pixels formation after setting the time to be similar to both sides of the detector.

The final step of the data analysis was the determination of the dead layer thickness. The actual results for the dead layer are shown below.

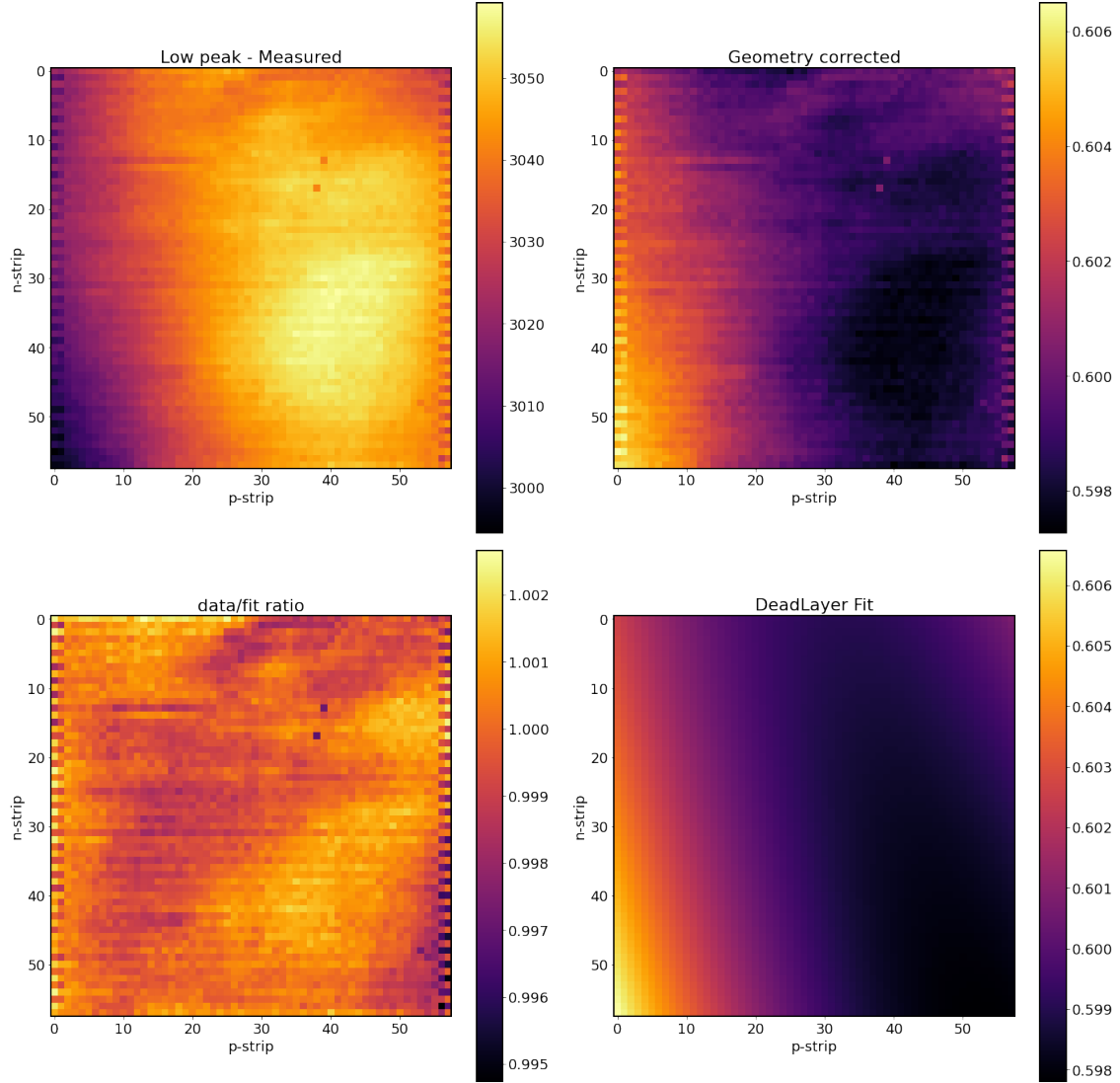


Figure 28: Visualisation of the results for the dead layer thickness using the ^{148}Gd source at 8.4 cm. The upper left plot shows the experimental pixel-gated calibrated energies obtained from the data taken with the ^{148}Gd source plotted in n- vs p-strip. The upper right plot is the dead layer thickness, which was obtained from the pySRIM calculations. The initial energy of the α particles radiating from the ^{148}Gd source is 3182.7(1) keV. By setting the initial energy to be 3182.7(1) keV and through an iterative method of modifying the dead layer thickness the final thickness was reached. The plot is “Geometry corrected” which means that we have already taken into account the apparent thicker dead layer due to the incident angle. A smooth polynomial function was used to fit the dead layer, which can be seen in the lower right part. The dead layer turned out not to be uniform, as expected, however, it is not random suggesting that the dead layer was created via a physical process, likely the evaporation of SiO_2 onto the surface. The lower left plot, shows the data-to-fit ratio and can be seen that it is approximately one.

5 Discussion

This thesis focused on the characterization of the implantation detector of LUNDIUM decay station. The dead layer was found to be in the order of $0.594\ \mu\text{m}$ - $0.602\ \mu\text{m}$, which resulted in a very thin dead layer. There is also evidence that the dead layer was produced via a physical process. Since the dead layer this time was calculated to be much less than usual, previous silicon detectors owned by the Nuclear Structure Group had a dead layer thickness of around $2\ \mu\text{m}$, the evaporation of silicon dioxide and the ion-implanted method are believed to have been done by a method which used a lower energy compared to before.

The value of the dead layer was determined with the experimental data obtained from the ^{148}Gd source placed at a distance of 8.4 cm away from the detector. One of the reasons that this source was used, was due to the fact that most of the particles would get influenced by the same amount the dead layer. For the actual determination of the dead layer thickness, only data with one source was needed. However, for crosschecking reasons, the ^{148}Gd source with data from a close distance (3.1 cm) was also chosen for determining the dead layer. In this case, since our source was positioned roughly 5 mm off-center in the y-direction, there was a corner that recorded no energies at all. The zero entries caused a problem in the compilation of the Jupyter notebook. Due to limited amount of time and since we already had valid results, the notebook problem was not fixed.

^{244}Cm instead was used for confirming the dead layer thicknesses values. However, in this case, during the calibration process, in the Gnuplot script, the energy of the ^{244}Cm source was set to $E = 5805\ \text{keV}$, which is the highest energy of the α particle. Instead the mean average of the two highest peaks should have been taken into account. This caused the calibrated values of the ^{244}Cm to not be correct. For fixing this, a new Gnuplot script was required that would fit four peaks instead of three. Since the energies were higher than expected, it couldn't be used for dead layer thickness determination. For our calibration, since two points were fixed (^{133}Ba and ^{148}Gd), the third point didn't change the calibration line significantly. Also, the energy difference for the Curium source was small enough, which had no effect when the thickness of the dead layer thickness was determined.

Throughout this thesis, the importance of the dead layer was highlighted. Figure 23 represents the importance of the angle of incidence when correcting for the energy loss in the dead layer. After calibrating the detector, the energy distribution over the strips is expected to resemble a straight line. As can be seen in Figure 23, the distribution is much more spread out, which is due to the angle of incidence. In this case, the geometrical factor should be taken into account for the energy reconstruction.

6 Conclusion & Outlook

Overall, this thesis illustrates the importance of the dead layer for nuclear spectroscopy experiments as well as it shows the detailed results for the dead layer thickness over the surface of the new implantation detector of LUNDIUM. The results of this report will be used for the data analysis towards a research publication. The data for the publication will be taken with the, currently being built, LUNDIUM decay station, planned in March 2022, in experiments that will be conducted at GSI.

For future work, the dead layer of the n-side of the detector can be calculated. Furthermore, an interesting consideration is to repeat the experiment with the source positioned exactly in the middle w.r.t the detector. Lastly, an important aspect for the dead layer is to try to get the pixels in the detector without requiring the time between the events to be within a 1 ns interval. As can be seen in Figures 26 and 27, one can see that the diagonal events on the pixel formation plot are much less than before. This might result in losing too many potential good hits.

References

- [1] Table of nuclides - Wikipedia [Internet]. En.wikipedia.org. 2021 [visited 30 November 2021]. Available from: https://en.wikipedia.org/wiki/Table_of_nuclides.
- [2] S  mark-Roth A., Spectroscopy along Decay Chains of Element 114, Flerovium, [Ph.D Thesis]. Lund University; ISBN: 78-91-7895-836-8; 2021.
- [3] Leo W., Techniques for Nuclear and Particle Physics Experiments: A How-to Approach. 1st ed. Berlin: Springer-Verlag; 1987.
- [4] Krane K., Introductory Nuclear Physics. 2nd ed. New York: John Wiley & Sons; 1988.
- [5] Hofmann P., Solid State Physics: An Introduction [Internet]. Weinheim: John Wiley & Sons; 2011 [visited 13 November 2021]. Available from: <https://lubcat.lub.lu.se/cgi-bin/koha/opac-detail.pl?biblionumber=6131918>
- [6] Sayed T., Assessment of the Capability for Vetoing Beta-Decay Events in the Lundium Decay Station [Bachelor Thesis]. Lund university; 2022.
- [7] Hrabar Y., *et al.* Anti-Compton shield for COMPEX germanium detector modules. [To be published]
- [8] Forsberg U., Element 115 [Ph.D]. Lund University; 2016.
- [9] Golubev P., *et al.* The Lund-York-Cologne Calorimeter (LYCCA): Concept, Design and Prototype Developments for a FAIR-NUSTAR Detector System to Discriminate Relativistic Heavy-ion Reaction Products. Nuclear Instruments & Methods in Physics Research. Section A: Accelerators, Spectrometers, Detectors, and Associated Equipment;723:55-66; 2013. <https://doi.org/10.1016/j.nima.2013.04.058>
- [10] Kurz N. The General Purpose Data Acquisition System MBS at GSI (and elsewhere). Presentation presented at GSI; 2016.
- [11] The Go4 Analysis Framework [Internet]. Web-docs.gsi.de. 2013 [visited 1 December 2021]. Available from: http://web-docs.gsi.de/~go4/go4V04/manuals/Go4introV4.htm#_Toc373306643
- [12] team R. ROOT: analyzing petabytes of data, scientifically. [Internet]. ROOT. [visited 1 December 2021]. Available from: <https://root.cern.ch/>
- [13] Farghaly D., Characterization of Double Sided Silicon Strip Detectors from LYCCA modules for FAIR [Bachelor Thesis]. Lund University; 2019.
- [14] Knoll G., Radiation Detection and Measurements. 1st ed. New York: John Wiley & Sons; 1979.
- [15] pysrim [Internet]. PyPI. [visited 1 December 2021]. Available from: <https://pypi.org/project/pysrim/>
- [16] James Ziegler - SRIM & TRIM [Internet]. Srim.org. [visited 1 December 2021]. Available from: <http://www.srim.org/>
- [17] gnuplot homepage [Internet]. Gnuplot.info. 1986 [visited 1 December 2021]. Available from: <http://www.gnuplot.info/>
- [18] Fusion 360 — 3D CAD, CAM, CAE & PCB Cloud-Based Software — Autodesk [Internet]. Autodesk.com. 2021 [visited 1 December 2021]. Available from: <https://www.autodesk.com/products/fusion-360/overview>

A Appendix

A.1 Fusion 360[©]

FUSION 360[©] is a 3D modelling tool that is used for product design as well as manufacturing [18]. In the beginning of this Bachelor thesis, the vacuum chamber that we used for the experiment along with some additional items were designed in this software platform. When the 3D vacuum chamber was completed, one made sure that the items that would be located inside the chamber would actually fit. A source holder was also designed, which was used for the experiment. The source holder was printed by a 3D printer, owned by the Nuclear Structure Group. Lastly, the profile items had to be arranged in such manner that the source would be able to be moved in three different directions (x , y , z). Render pictures from the vacuum chamber, the source holder and the source stand are shown below.

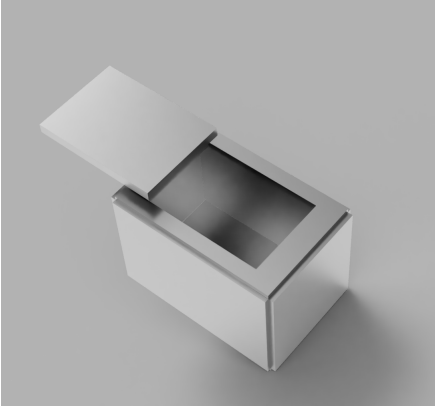


Figure 29: The vacuum chamber used for this experiment as designed in Fusion 360.



Figure 30: The item profiles joint together and the source positioned vertically.

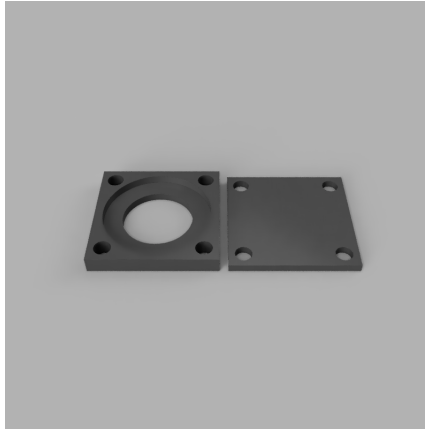


Figure 31: The source holder designed. Since the source holder was positioned vertically, a lid was sketched for the source safety.

A.2 Mapping

As mentioned above, the mapping between hardware and software of the detector is vital for knowing the position of the particles when hitting the detector. During the determination of the dead layer thickness, the mapping step verifies that the detectors were cabled in the right order. The raw hit pattern of energies can be seen below. We expected the height to increase smoothly as the channels and the FEBEX cards increased.

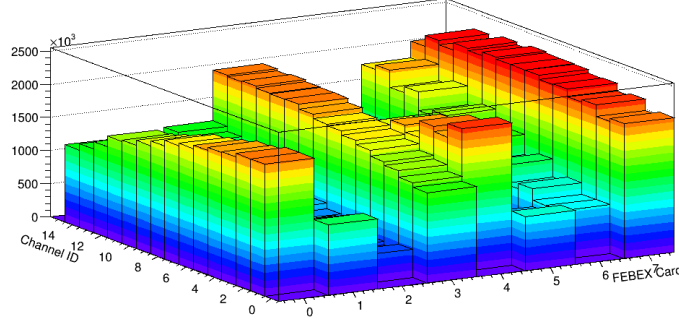


Figure 32: Raw hit pattern of energies for the ^{148}Gd source positioned close to the detector.

Because of the inconsistent pattern, our first thought was to swap cards 2 and 3 with 0 and 1. In the same way for the n-side [4, 5, 6, 7], cards 6 and 7 were swapped with cards 4 and 5. This led to a gaussian pattern which seemed correct (Figure 33), however the consequent results and plots did not agree with our expected data. After some investigation, we figured out that the low numbers in the cables in the detector go to high numbers in the preamplifiers output. More specifically, in each PCB, there are two FEBEX cards connected and the card channel 0 actually read channel 32. Furthermore, the PCB reads the n-side of the detector in a “off by one” channel (0 & 1 are swapped, 2 & 3 are swapped etc).

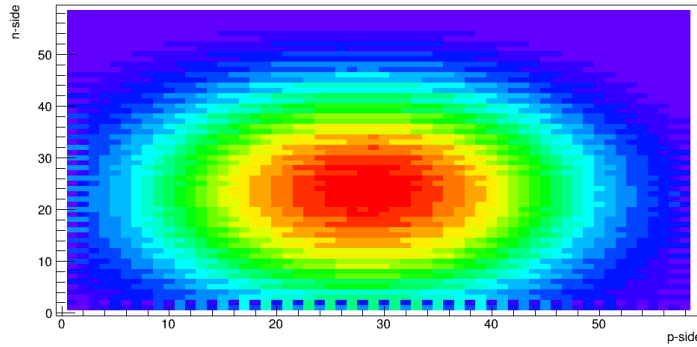


Figure 33: 2D hit pattern for ^{148}Gd , after the FEBEX cards were swapped. It is clear that the Y direction (n-side) shows a non smooth behavior that needed fixing.



Figure 34: The PCB where the cables from the detectors are soldered to.

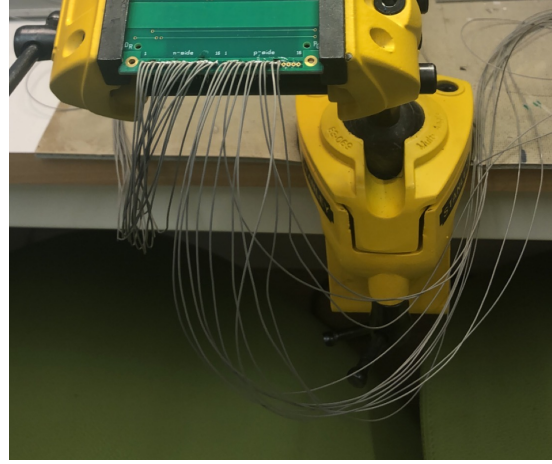


Figure 35: Picture used for showing the bonding of the cables in the detectors.

Another way to verify that the cabling was done in the right way was to apply a mask to the detector as can be seen below. In this way, the α particles are stopped in the paper and a “shadow” should be seen in the detector.

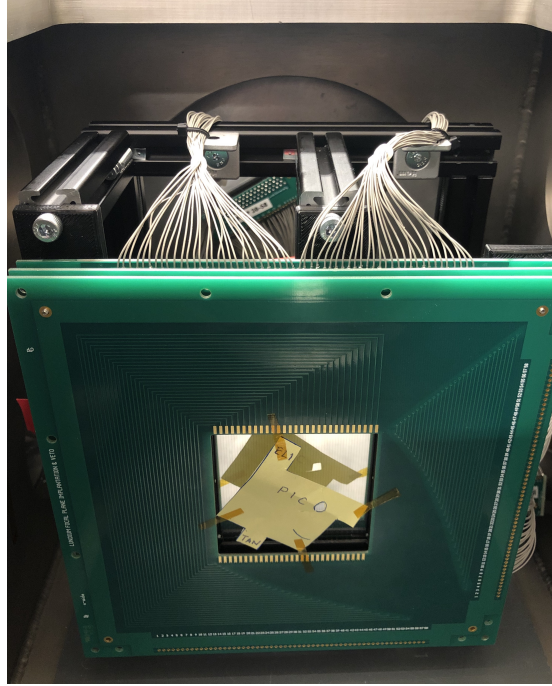


Figure 36: A mask applied in front of the detector.

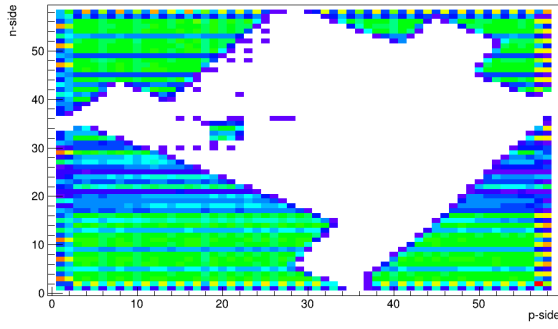


Figure 37: 2D hit pattern obtained in strip numbers using the mask. The pattern looks rotated 180° due to the orientation of the implantation detector.

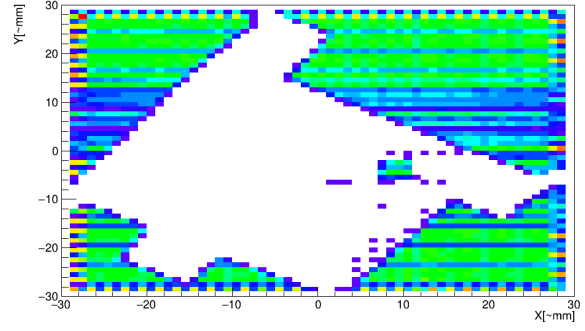


Figure 38: 2D hit pattern of the detector using the mask, mapped in real (x , y) space. The pattern is similar in direction with that in Figure 36, verifying that the mapping step was done correctly. For this mapping, the incorrect behavior on the n-side in Figure 33 has been corrected for.

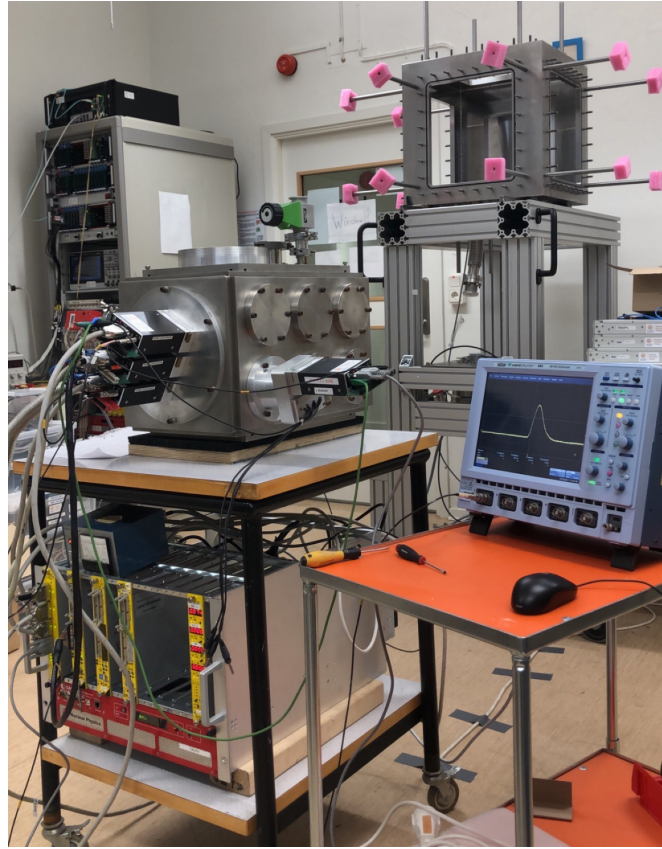


Figure 39: A picture from the lab, showing the vacuum chamber connected to the oscilloscope, to observe the signals. The LUNDIUM frame can be seen on the background, with the pink safety foam.